International Journal of Rock Mechanics & Mining Sciences 157 (2022) 105178

Contents lists available at ScienceDirect

International Journal of Rock Mechanics and Mining Sciences

journal homepage: www.elsevier.com/locate/ijrmms

A method for full three-dimensional kinematic analysis of steep rock walls based on high-resolution point cloud data

Giovanni Gigli, Luca Lombardi, Tommaso Carlà *, Tommaso Beni, Nicola Casagli

Department of Earth Sciences, Università degli Studi di Firenze, Via Giorgio La Pira 4, 50121, Florence, Italy

ARTICLE INFO

Keywords:
Rockfall susceptibility
Three-dimensional kinematic analysis
High-resolution point cloud
Terrestrial laser scanner
Semi-automatic discontinuity mapping

ABSTRACT

The predisposition of a slope to generate rockfalls is related to the intensity of rock mass jointing and the geometric arrangement of discontinuities intersecting the rock face. With the increasing use of terrestrial laser scanner (TLS) in rock slope surveying, methods have been proposed to semi-automatically extract the spatial properties of outcropping discontinuities from high-resolution topographic data. The present paper builds upon one of such methods (named DiAna), and extends it to enhance the assessment of rockfall susceptibility over steep rock walls. In particular, a Matlab routine (named DiAna-K) that incorporates a full three-dimensional derivation of kinematic analysis principles is introduced. Kinematic tests for plane, wedge, block toppling, flexural toppling, and free fall failure are formulated by explicitly accounting for the presence of overhanging areas of the rock face as well as varying frictional strengths across different discontinuity sets, planes, or intersections between planes. Results from a test application at an abandoned quarry site highlight the ability of the proposed procedure to provide detailed insights into the kinematic feasibility of structurally controlled instabilities. They also demonstrate the importance of properly defining failure mechanisms over steep (and usually undersampled) topographies in order to derive realistic quantifications of rockfall hazards.

1. Introduction

Steep rock walls are characterized by a marked predisposition to rockfall, which is defined as the detachment and subsequent fall, bouncing, rolling, sliding, and deposition of rock fragments under the influence of gravity.[1] As opposed to the flow-like behavior of rock avalanches, rockfalls show no significant interaction between individual particles, meaning that their downslope propagation can be simulated by numerical models based on rigid body ballistics.[2] This type of landslide represents a major hazard across most populated mountain landscapes and surface mining operations, affecting high slopes as well as single bedrock outcrops. It may originate as a result of a wide variety of slope instability mechanisms, involving from single pebbles to catastrophic failure of thousands of cubic meters.[3,4]

The management of rockfall hazards and associated risks primarily depends on the knowledge of the whereabouts and timing of rockfall triggering. The timing is typically elusive: while accelerating displacements leading to slope collapse and ensuing rockfall have been reported,[5–7] precursors are undetectable or very short-lived when instabilities are relatively small in volume and/or in hard rocks. Many authors have therefore focused their attention on the concept of rockfall susceptibility, namely the estimation of how likely rockfalls are at a specific site—from the scale of single slopes to entire valleys. In this sense, approaches can be broadly divided into two categories: frequency–magnitude distributions of future rockfall occurrence may be inferred from geological/morphometric parameters[8–12] and the compilation of rockfall inventories[4,13–17]; alternatively, location and type of source mechanisms may be evaluated through explicit consideration of rock mass structure.[18–21] The latter approach is rooted in the notion that the development of failure mechanisms is largely governed by the intensity of rock mass jointing and the geometric arrangement of discontinuities intersecting the rock face. The tendency to instability may then be expressed in terms of factors of safety derived from deterministic/stress-strain solutions (e.g., limit equilibrium, discrete element), or in terms of the kinematic feasibility of block movement (e.g., kinematic analysis). Deterministic/stress-strain solutions are numerically more rigorous, but have a narrower applicability (usually limited to the analysis of selected rock compartments) and must be constrained by input data from extensive laboratory testing and fieldwork. Methods predicated on the principles of stereographic-based

* Corresponding author.
E-mail address: tommaso.carla@unifi.it (T. Carlà).

https://doi.org/10.1016/j.ijrmms.2022.105178
Received 4 October 2021; Received in revised form 9 May 2022; Accepted 11 July 2022
Available online 18 July 2022

Fig. 1. High-resolution true-colored point cloud of the quarry test site.

kinematic analysis, which aim to identify where the kinematic conditions for block detachment are theoretically met, can rather be applied expeditiously at the scale of entire slopes.

Advanced surveying instruments such as terrestrial laser scanner (TLS) have now become common tools for the creation of high-resolution three-dimensional models of steep rocky slopes, from which not only the morphology of the terrain, but also orientation and other relevant discontinuity properties can be extracted.[22–24] This has proved to be invaluable in vast, dangerous, or otherwise inaccessible scenarios, where traditional scanline surveying cannot be carried out. Discontinuity planes may be mapped either on polygonal meshes or directly on raw point cloud data, and typically in much greater number than what is practically achievable with traditional methods. Fitting routines may require manual input from the user[25] or be semi-automatic. To cite just a few examples from the second group, Vöge et al.[26] developed a series of algorithms to identify discontinuity planes based on the angular deviation of the nodes of polygonal meshes. Riquelme et al.[27] proposed a method for grouping discontinuity sets in point cloud data by means of a kernel density estimation and outlining single discontinuities by means of a density-based clustering algorithm. Matasci et al.[21] presented a successful application of the Coltop3D code, which allows the definition of discontinuity sets by computing dip and dip direction of each point in the cloud with respect to a set of neighbors.

This increased capability of collecting topographic and rock mass structural data now makes it possible to also refine the thoroughness of kinematically-based rock slope stability assessments. The present paper focuses on the enhanced quantification of rockfall hazards in steep rock walls by exploiting high-resolution point cloud data acquired from terrestrial laser scanning. The proposed analysis workflow is the outcome from a decennial research effort on the topic and multiple field experiences.[28–35] Building upon the semi-automatic extraction of key discontinuity properties by means of the established DiAna[29] (Discontinuity Analysis) approach, an upgraded Matlab routine (named DiAna-K) is introduced to calculate the probability of structurally controlled instabilities based on an extended three-dimensional derivation of kinematic analysis principles. Indexes of rockfall susceptibility are conceived to explicitly account for the presence of overhanging surfaces—where failure of rock in tension may produce free fall mechanisms—and specific friction coefficients for discontinuity sets, planes, or lines of intersection between planes. The term "*overhanging*" is herein adopted to indicate a jutting portion of the rock wall that, contrarily to "*normal*" rock wall areas, is oriented in the direction of lower elevation. The main features of the method are highlighted by surveying a steep rock wall at an abandoned quarry near the town of Florence (Central Italy) historically affected by rockfall hazards.

2. Materials and methods

2.1. Test site and TLS survey

The method described in the next paragraphs was applied at the rock wall of an abandoned quarry 5 km N of the town of Florence (Central Italy). The SSW–NNE trending sub-vertical quarry face, with a height of ~25 m and a width of ~70 m, was excavated into Oligocene–Miocene foredeep turbidites belonging to the Macigno Formation, consisting of an alternation of medium to thick beds (up to 10 m) of coarse-grained sandstones and thin, more sporadic beds of finer grained pelitic deposits. Instability mechanisms of different type and size arise from the changing mechanical strength and tendency to weathering across the various bedding strata, which are systematically intersected by high-angle discontinuities. A RIEGL VZ1000 terrestrial laser scanner was employed to collect high-resolution point clouds of the quarry face with a mean spacing of 8 mm. Occlusions were reduced by performing acquisitions from two different points of view, with a distance from the rock wall of 25–30 m. Six marker reflectors were distributed across the quarry floor, and their coordinates were surveyed with a geodetic Global

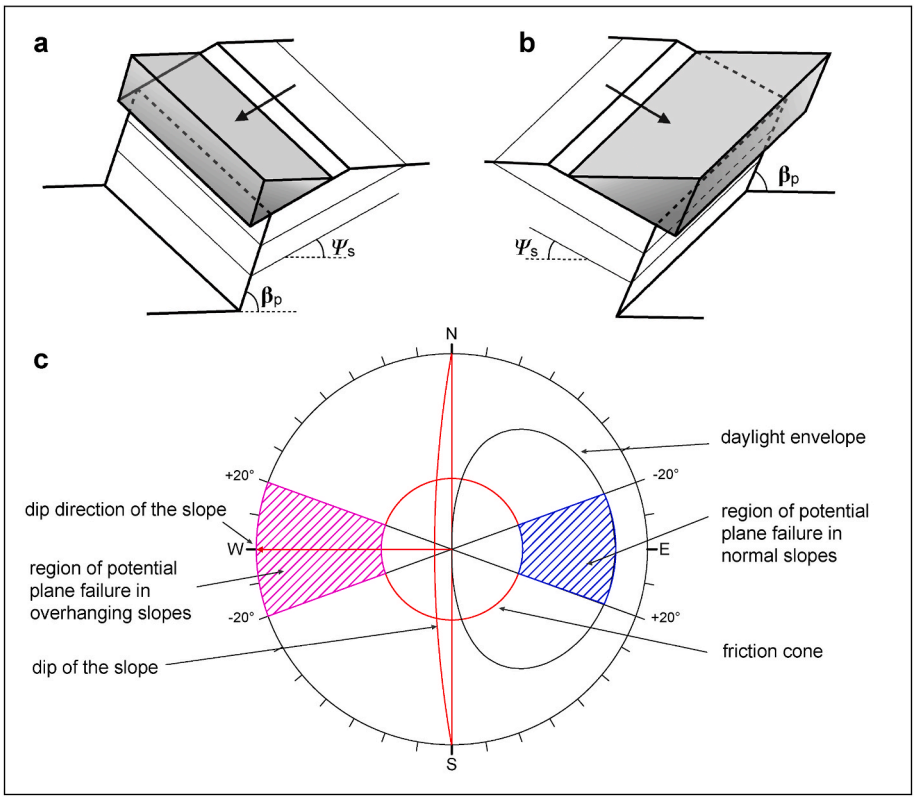

Fig. 2. Schematic illustration of plane failure in normal (a) and overhanging (b) slopes, with resulting kinematic analysis based on a lower hemisphere equal angle stereonet (c). Regions of kinematic feasibility are identified by assuming a dip/dip direction of the slope of 80°/270° and a friction angle along the basal discontinuity of 30°.

Navigation Satellite System (GNSS) receiver. This operation allowed the correct alignment and georeferencing of the point clouds. During the scan, an integrated Nikon D700 camera captured a series of partially overlapping panoramic photographs that were subsequently stitched together in order to drape the three-dimensional model of the rock wall with its true colors. The final merged point cloud, generated through use of the RiSCAN PRO software package, is composed of more than 100 million points (Fig. 1). The related polygonal mesh covers an area of 1043.42 m^2, with a mean mesh element size of 2.06 × 10^{-3} m^2.

2.2. Brief overview of DiAna and derivation of full three-dimensional kinematic analysis (Diana-K)

Modes of failure across rocky slopes can be examined using the principles of stereographic-based kinematic analysis. Developed by several authors,[28,36–41] kinematic analysis of block stability is aimed at identifying the areas of the rock face where the geometric arrangement of discontinuities renders a structurally controlled failure kinematically feasible. The approach is highly instrumental in predicting the most probable rockfall source areas and designing appropriate containment measures. Discontinuities are assumed to be infinitely persistent, and the contribution to the joint shear strength to be exclusively due to friction. The quality of outputs is naturally influenced by how well the sampled discontinuities reproduce the actual rock mass configuration. Here, an established semi-automatic approach named DiAna (Discontinuity Analysis)[29] was used to map discontinuities at the test site and extract six of the associated key parameters suggested by ISRM[42] for their quantitative description—namely orientation, JRC, number of sets, spacing/frequency, persistence, and block size. Of these, the first two can be directly inputted in subsequent kinematic analysis. Nonetheless, the kinematic tests built into the upgraded Diana-K routine may also be run by inputting discontinuity properties collected through traditional geomechanical surveying or other semi-automatic methods. Likewise, other techniques (e.g., photogrammetric surveying) may be used to input topographic data into DiAna and DiAna-K; but, in the authors' experience, TLS surveys are best able to model sharp edges and rough surfaces, which so fundamentally characterize jointed sub-vertical rock walls.

In short, the rationale of the original DiAna routine[29] consists in the creation of a voxel of space in the form of a searching cube that is iteratively moved over the raw point cloud. A least-squares fitting plane is then assigned to each sub-group of points. The user is required to select a threshold value for the standard deviation of the best fitting plane, on the basis of which the algorithm decides whether this corresponds to a valid cluster. The appropriate threshold is calibrated empirically according to searching cube size, point cloud resolution, and rock face roughness. The searching cube must contain a predefined minimum number of points—also function of point cloud resolution—to avoid small unrepresentative clusters. Once a valid cluster is identified, dip (α_p) and dip direction (β_p) of the fitting plane are calculated from:

$$\alpha_p = \arctan\left(\frac{m}{l}\right) + Q \tag{1}$$

$$\beta_p = \arctan\left(\frac{n}{\sqrt{l^2 + m^2}}\right) \tag{2}$$

where l, m, and n are the direction cosines of the plane, while Q is a constant given by: $Q = 0°$ if $l > 0$ and $m > 0$; $Q = 360°$ if $l > 0$ and $m < 0$; $Q = 180°$ if $l < 0$ and $m < 0$, or $l < 0$ and $m > 0$. Clusters belonging to adjoining searching cubes and the same discontinuity set are interpreted as being part of the same discontinuity plane, and are therefore merged together. At the same time, the searching cube must be of sufficiently small size to prevent clusters belonging to two closely-spaced parallel discontinuities from being merged together. The

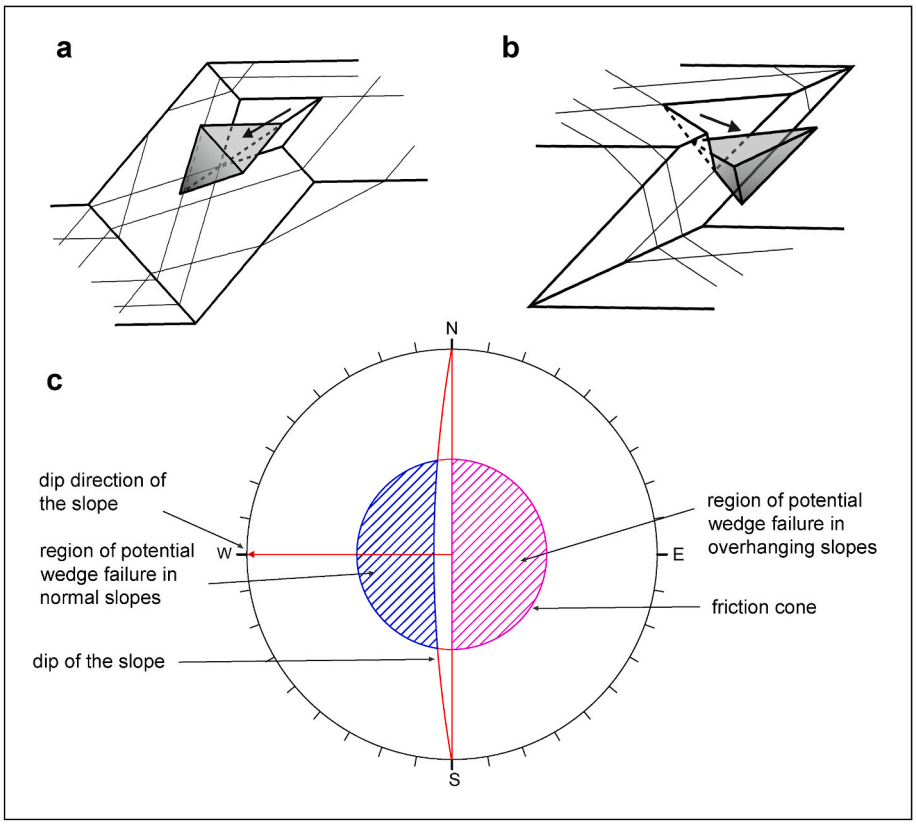

Fig. 3. Schematic illustration of wedge failure in normal (a) and overhanging (b) slopes, with resulting kinematic analysis based on a lower hemisphere equal angle stereonet (c). Regions of kinematic feasibility are identified by assuming a dip/dip direction of the slope of 80°/270° and an average friction angle along the intersection of the two discontinuities of 30°.

complete discontinuity bounding polygons are eventually drawn by applying a convex hull algorithm.

In Diana-K, after extraction of the discontinuity properties, kinematic tests are run by singling out the terrain mesh elements, the sampled discontinuity planes, and the lines of intersection between planes that are geometrically acceptable. In other words, through an iterative process, the orientation of each mesh element is evaluated against the orientation of each sampled discontinuity plane/intersection (or possible combination thereof). This provides additional context for the quantification of rockfall hazards, as opposed to solely making reference to the mean orientation of discontinuity sets or tightly clustered discontinuity orientations. Another notable feature is that, as the input topography is meshed from a point cloud, failure mechanisms can also be evaluated by means of dedicated kinematic tests for overhanging rock wall areas. Sets of equations describing kinematic feasibility in "*overhanging*" slopes can in fact be derived from simple stereographic-based arguments (Figs. 2–6). This allow expanding the scope of standard guidelines for kinematic analysis, whose formulation has been limited to "*normal*" slopes[41] mostly because: i) the method is widely employed in excavation and surface mining projects, where rock slope designs almost never entail overhanging geometries; and ii) terrain elevation data from aerial topographic surveying—of common use as analysis input—are unable to capture overhanging geometries. The extended kinematic tests built into Diana-K (see Paragraphs 2.2.1–2.2.5) include consideration of plane, wedge, block toppling, flexural toppling, and free fall failure mechanisms, with free fall only being feasible in overhanging rock wall areas where pure tension controls block detachment (i.e., no contribution of friction and no block sliding or rotation). In accordance with suggestions by Matheson[38,39] and Hudson and Harrison,[40] distinct friction angles may be assigned to planes/intersections.

At the test site, a traditional geomechanical survey was conducted along a sample scanline at the bottom of the quarried slope to acquire measurements of JRC and rebound number from Schmidt hammer testing. Discontinuities were observed to be rough and planar, with JRC measurements falling in the range 4–10. Such values are consistent with those extracted from DiAna, which does so by moving searching cubes of varying size along the selected discontinuity trace and measuring the scatter in dip and dip direction of locally fitted planes.[29] As the rock mass has relatively small extent and consistent strength properties, for convenience an average value of total friction angle (φ) was assigned to each discontinuity set (Fig. 7) following the simplified Maksimović's relation[43] for low normal stress levels:

$$\varphi = \varphi_b + 2JRC \tag{3}$$

where φ_b is the basic friction angle (whose values were inferred from literature data on similar rock types).[44] A more selective assignment of friction angles is unnecessary for the present aim of illustrating the operational aspects of Diana-K. Moreover, as bedding moderately dips into the slope and friction is mainly mobilized along the other sets of joints dipping steeply out of the slope (Fig. 7), strength differences between these two types of discontinuity are deemed to have a minor influence on the analysis results.

2.2.1. Plane failure

Plane failure involves sliding of the block along a basal discontinuity plane dipping out of the slope (Fig. 2). The upper end of the sliding surface is assumed to either intersect the less steep upper slope or terminate in a tension crack.[41] If the constraint provided by lateral margins is ignored, the conditions required for plane failure in "*normal*" mesh elements are:

$$\alpha_s - 20^\circ < \alpha_p < \alpha_s + 20^\circ \tag{4}$$

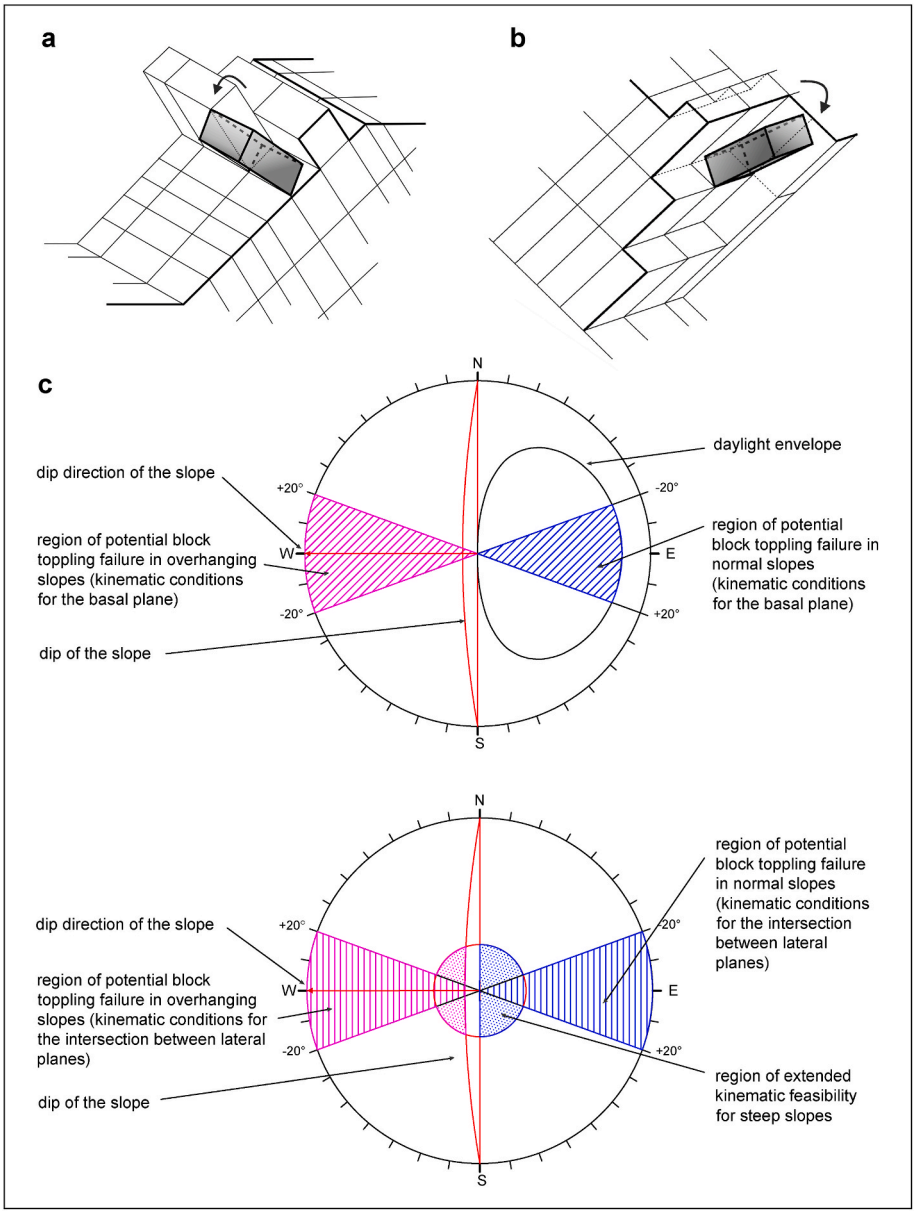

Fig. 4. Schematic illustration of block toppling failure in normal (a) and overhanging (b) slopes. Resulting kinematic analysis is based on lower hemisphere equal angle stereonets (c), and depicts the conditions for the basal discontinuity (upper stereonet) and the intersection of the lateral discontinuities (lower stereonet). Regions of kinematic feasibility are identified by assuming a dip/dip direction of the slope of 80°/270° and a friction angle along the intersection of the lateral discontinuities of 30°.

$$\beta_p < \psi_s \tag{5}$$

$$\beta_p > \varphi \tag{6}$$

where α_s is the dip direction of the slope, α_p the dip direction of the discontinuity plane, β_p the dip of the discontinuity plane, $\psi_s = \arctan(\tan\beta_s \cos|\alpha_s - \alpha_p|)$ the apparent dip of the slope along the dip direction of the discontinuity plane (as derived from the true dip of the slope β_s), and φ the available frictional strength along the discontinuity plane. In "*overhanging*" mesh elements, besides the dip of the basal plane being greater than the friction angle (Eq. (6)), the other required condition is:

$$(\alpha_s \pm 180°) - 20° < \alpha_p < (\alpha_s \pm 180°) + 20° \tag{7}$$

At any given element of the polygonal mesh, the susceptibility to plane failure (S_{pf}) is:

$$S_{pf} = N_{pf}/N\ (\%) \tag{8}$$

where N_{pf} is the number of discontinuity planes satisfying Eqs. (4)–(6) in "*normal*" mesh elements or Eqs. (6) and (7) in "*overhanging*" mesh elements, and N is the total number of mapped discontinuity planes.

2.2.2. *Wedge failure*

Kinematic analysis of wedge failure requires appraisal of the geometry of two mutually intersecting discontinuity planes (Fig. 3). The conditions that must be satisfied for wedge failure to occur in "*normal*" mesh elements are:

$$\alpha_s - 90° < \alpha_i < \alpha_s + 90° \tag{9}$$

$$\beta_i < \psi_s \tag{10}$$

$$\beta_i > \varphi_{eq} \tag{11}$$

where α_i is the dip direction of the line of intersection between the two planes, β_i the dip of the line of intersection between the two planes, $\psi_s = \arctan(\tan\beta_s \cos|\alpha_s - \alpha_i|)$ the apparent dip of the slope along the dip direction of the line of intersection between the two planes, and φ_{eq} is the equivalent friction angle. The use of the equivalent friction angle derives from the observation that, by simply using the mean friction

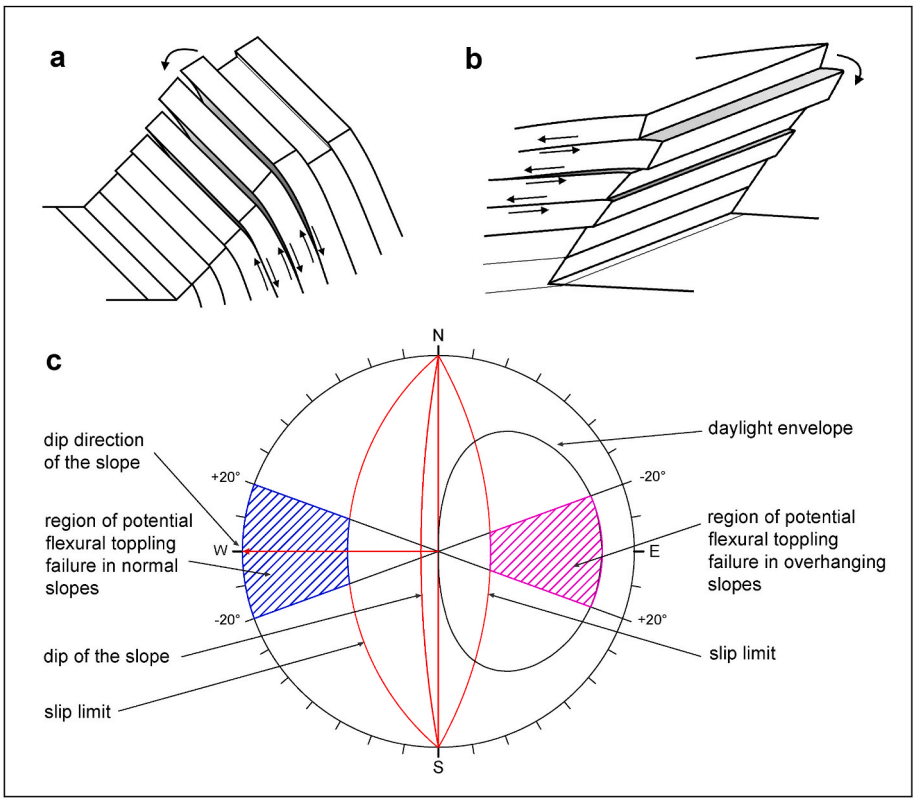

Fig. 5. Schematic illustration of flexural toppling failure in normal (a) and overhanging (b) slopes, with resulting kinematic analysis based on a lower hemisphere equal angle stereonet (c). Regions of kinematic feasibility are identified by assuming a dip/dip direction of the slope of 80°/270° and a friction angle along the steep discontinuity of 30°.

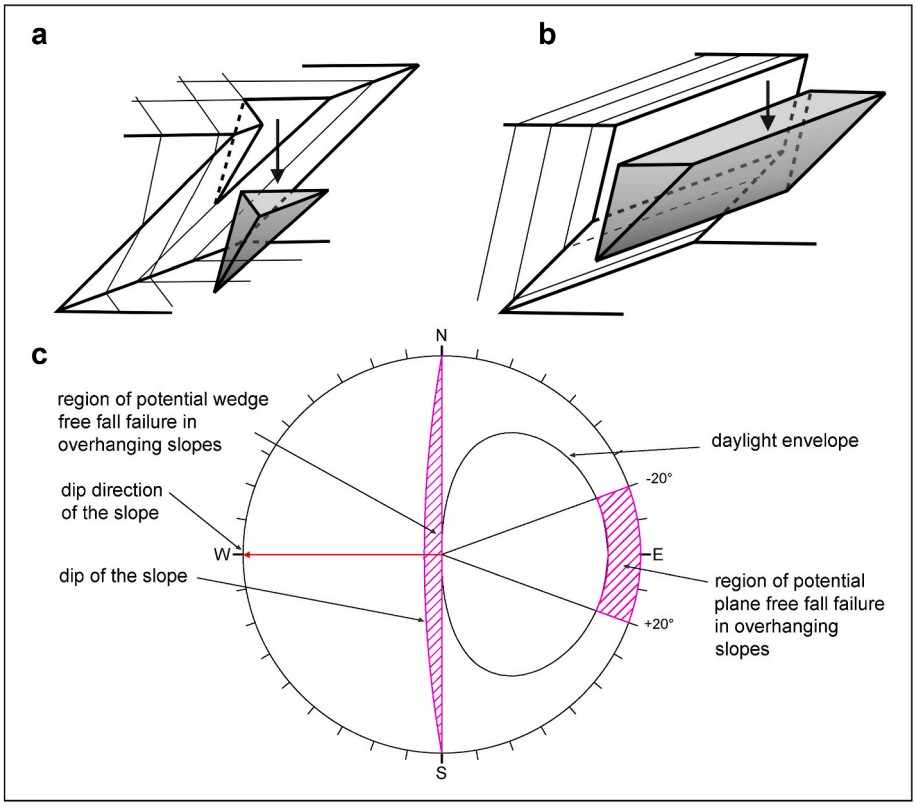

Fig. 6. Schematic illustration of wedge free fall failure (a) and plane free fall failure (b) in overhanging slopes, with resulting kinematic analysis based on a lower hemisphere equal angle stereonet (c). Regions of kinematic feasibility are identified by assuming a dip/dip direction of the slope of 80°/270°.

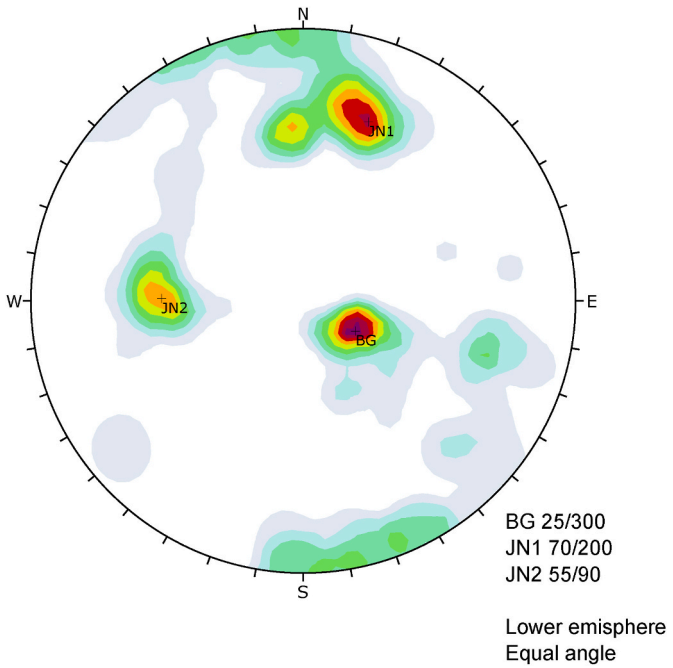

Fig. 7. Contour plot of poles to discontinuities extracted from DiAna, represented on a lower hemisphere equal angle stereonet. BG: Bedding. JN1: Joint set 1. JN2: Joint set 2.

angle of the two discontinuity planes (and therefore by strictly likening wedge failure to sliding of a block along the line of intersection between two discontinuity planes), Eqs. (9)–(11) would be disproportionately biased towards safety.[37,41] In reality, stability is also controlled by the details of the geometry of the wedge, which can be expressed by the wedge factor K according to:

$$K = \frac{\sin\chi}{\sin\xi/2} \tag{12}$$

where χ is the angle of tilt of the wedge, as seen in the plane perpendicular to the line of intersection; and ξ is the included angle of the wedge, again as seen in the plane perpendicular to the line of intersection.[41] The equivalent friction angle is thus computed from:

$$\tan\varphi_{eq} = K\tan\overline{\varphi_i} \tag{13}$$

where $\overline{\varphi_i}$ is the average friction angle along the line of intersection resulting from the contribution of χ, ξ, and the friction angles φ_1 and φ_2 along the two discontinuity planes according to:

$$\tan\overline{\varphi_i} = \left[\frac{1}{2} + \frac{\tan(\xi/2)}{2\tan\chi}\right]\tan\varphi_1 + \left[\frac{1}{2} - \frac{\tan(\xi/2)}{2\tan\chi}\right]\tan\varphi_2 \tag{14}$$

In "*overhanging*" mesh elements, wedge failure may occur if Eq. (11) is verified and Eq. (9) is reformulated into:

$$\alpha_s + 90^\circ < \alpha_i < \alpha_s - 90^\circ \tag{15}$$

At any given element of the polygonal mesh, the susceptibility to wedge failure (S_{wf}) is:

$$S_{wf} = I_{wf}/I\ (\%) \tag{16}$$

with I_{wf} being the number of intersections satisfying Eqs. (9)–(11) in "*normal*" mesh elements or Eqs. (11) and (15) in "*overhanging*" mesh elements, and I the total number of geometrically acceptable intersections.

2.2.3. Block toppling

Block toppling involves rotation of the displaced block about a fixed base. This mechanism typically recurs in bedded sandstone and columnar basalt formations where orthogonal jointing is well developed. Individual columns are defined by three sets of discontinuities (Fig. 4): two sets dipping steeply into the slope (i.e., sides); and a widely spaced set gently dipping out of the slope (i.e., base).[41] In Diana-K, sliding along the basal discontinuity may occur in addition to rotation (block-sliding toppling). The required conditions for block toppling concern the orientation of both the basal plane (α_p;β_p) and the line of intersection (α_i;β_i) between the two sets of lateral planes. For "*normal*" mesh elements, these are enunciated as follows:

$$\alpha_s - 20^\circ < \alpha_p < \alpha_s + 20^\circ \tag{17}$$

$$\alpha_s - 20^\circ < (\alpha_i \pm 180^\circ) < \alpha_s + 20^\circ \tag{18}$$

$$\beta_p < \psi_s \tag{19}$$

where in this case φ denotes the available frictional strength along the basal plane, which must be greater than the dip of the basal plane if block sliding is to be avoided. For "*overhanging*" mesh elements, conditions (17–19) respectively turn into:

$$\alpha_s - 20^\circ < (\alpha_p \pm 180^\circ) < \alpha_s + 20^\circ \tag{20}$$

$$\alpha_s - 20^\circ < \alpha_i < \alpha_s + 20^\circ \tag{21}$$

$$\beta_i < \psi_s \tag{22}$$

As shown in Fig. 4, in mesh elements where

$$\beta_i > 90^\circ - \varphi \tag{23}$$

the kinematic feasibility of block toppling may be extended by accepting the condition[28]

$$\alpha_s - 90^\circ < (a_i \pm 180^\circ) < \alpha_s + 90^\circ \tag{24}$$

The equation expressing the susceptibility to block toppling failure (S_{btf}) at any given element of the polygonal mesh is:

$$S_{btf} = \frac{N_{btf}}{N}\frac{I_{btf}}{I}\ (\%) \tag{25}$$

where N_{btf} is the number of discontinuity planes satisfying Eqs. (17) and (19) in "*normal*" mesh elements or Eq. (20) in "*overhanging*" mesh elements, N the total number of mapped discontinuity planes, I_{btf} the number of intersections satisfying Eq. (18) in "*normal*" mesh elements or Eqs. (21) and (22) in "*overhanging*" mesh elements, and I the total number of geometrically acceptable intersections.

2.2.4. Flexural toppling

Flexural toppling is distinguished by block toppling because it lacks a well-defined plane at the base of the rock columns, which are mutually separated by at least one set of steeply dipping discontinuities. This mechanism involves rear tensile failure and interlayer slip of the rock columns as they bend forward (Fig. 5).[41] Typical examples are thinly bedded rock masses in shale and slate in which orthogonal jointing is poorly developed. Kinematic analysis of flexural toppling is unable to account for the rock tensile strength, however the geometric conditions that favor its occurrence have been extrapolated by Goodman.[36] In Diana-K, concerning "*normal*" mesh elements and the set of steeply dipping discontinuities (α_p;β_p), these are written in the form:

$$\alpha_s - 20^\circ < (\alpha_p \pm 180^\circ) < \alpha_s + 20^\circ \tag{26}$$

$$\beta_p > \varphi + (90^\circ - \psi_s) \tag{27}$$

where in this case ψ_s is the apparent dip of the slope along the dip direction of the steep discontinuity. For "*overhanging*" mesh elements, conditions are rewritten as follows:

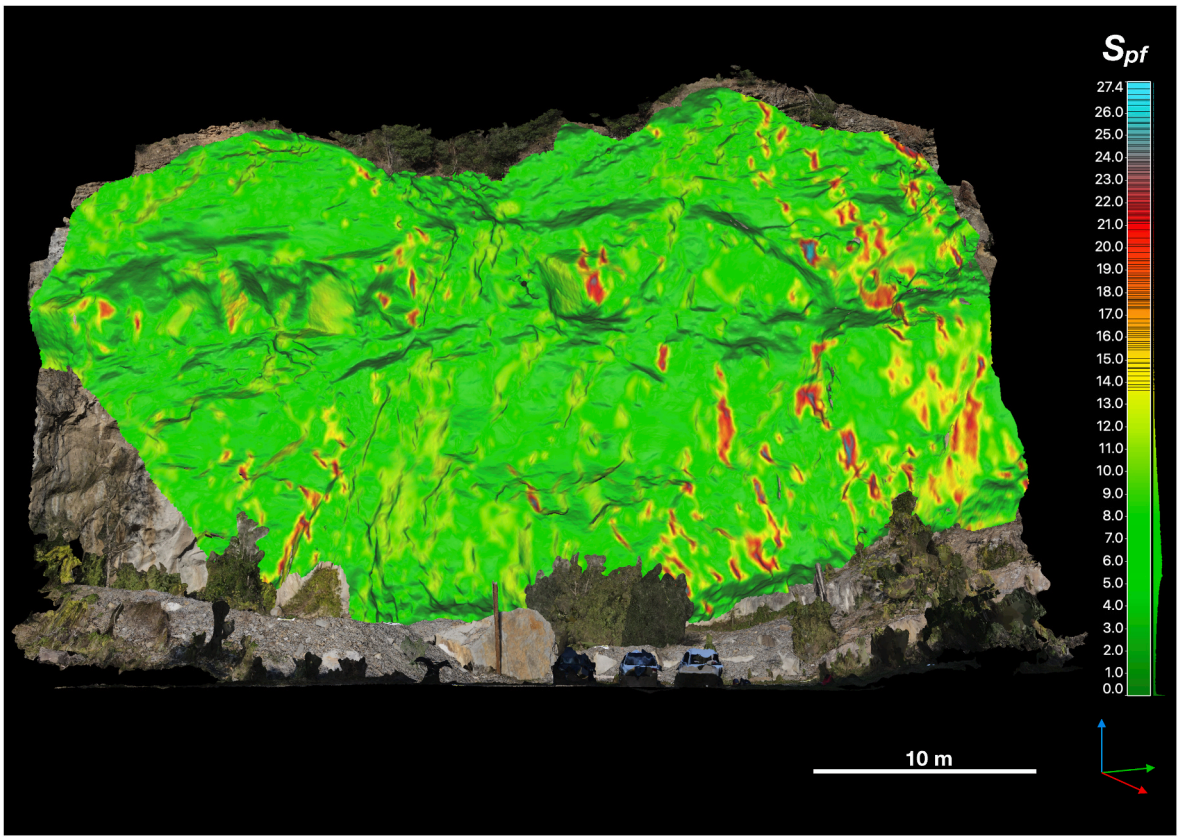

Fig. 8. Calculated susceptibility to rockfalls induced by plane failure at each element of the polygonal mesh. Results are superimposed on the point cloud of the quarry slope.

$$\alpha_s - 20^\circ < \alpha_p < \alpha_s + 20^\circ \tag{28}$$

$$\beta_p > \varphi + (\psi_s - 90^\circ) \tag{29}$$

$$\beta_p < \psi_s \tag{30}$$

At any given element of the polygonal mesh, the susceptibility to flexural toppling failure (S_{ftf}) is expressed by:

$$S_{ftf} = N_{ftf}/N\ (\%) \tag{31}$$

with N_{ftf} being the number of discontinuity planes that satisfy Eqs. (26) and (27) in "*normal*" mesh elements or Eqs. (28)–(30) in "*overhanging*" mesh elements, and N the total number of mapped discontinuity planes.

2.2.5. Free fall

Free fall excludes any component of sliding or rotational movement of the displaced block. Detachment occurs through pure tensile failure along at least a discontinuity (or line of intersection between discontinuities) that is steeper than the rock face; that is, the rock face must be oriented in the direction of lower elevation ("*overhanging*") and the geometric arrangement of discontinuities adhere to the classification of underdip cataclinal slopes by Cruden.[45] Depending on whether a single plane is affected by tension or an intersection between planes is also involved, further distinction may be made between plane free fall failure and wedge free fall failure (Fig. 6). The required kinematic conditions for free fall can thus be expressed by:

$$\alpha_s - 20^\circ < \alpha_p < \alpha_s + 20^\circ \tag{32}$$

$$\beta_p > \psi_s \tag{33}$$

or, alternatively, by:

$$\alpha_s - 90^\circ < \alpha_i < \alpha_s + 90^\circ \tag{34}$$

$$\beta_i > \psi_s \tag{35}$$

As a result, at any given element of the polygonal mesh, the overall susceptibility to free fall failure (S_{fff}) is estimated according to:

$$S_{fff} = 1 - \left(1 - S_{pfff}\right)\left(1 - S_{wfff}\right) \tag{36}$$

where S_{pfff} and I_{wfff} are the susceptibilities to plane free fall failure and wedge free fall failure, respectively. These two parameters are in turn calculated from:

$$S_{pfff} = N_{fff}/N \tag{37}$$

$$S_{wfff} = I_{fff}/I \tag{38}$$

with N_{fff} being the number of discontinuity planes that satisfy Eqs. (32) and (33) and I_{fff} the number of intersections that satisfy Eqs. (34) and (35). Again, N and I are the total number of mapped discontinuities and intersections, respectively.

3. Results

The aforementioned kinematic tests help define the rock wall areas that are more prone to structurally controlled instability, namely the areas where rockfall hazard is greater. The susceptibility to rockfalls due to a certain failure mechanism can be visually assessed by draping the polygonal mesh according to a color ramp. The color of each mesh element is determined by the locally computed value, on a range from 0% to 100%, of the susceptibility index in question (as derived from Eqs. ((8), (16), (25), (31) and (36)). In general, there is no objective way to determine what constitutes a high or low rockfall susceptibility, as this

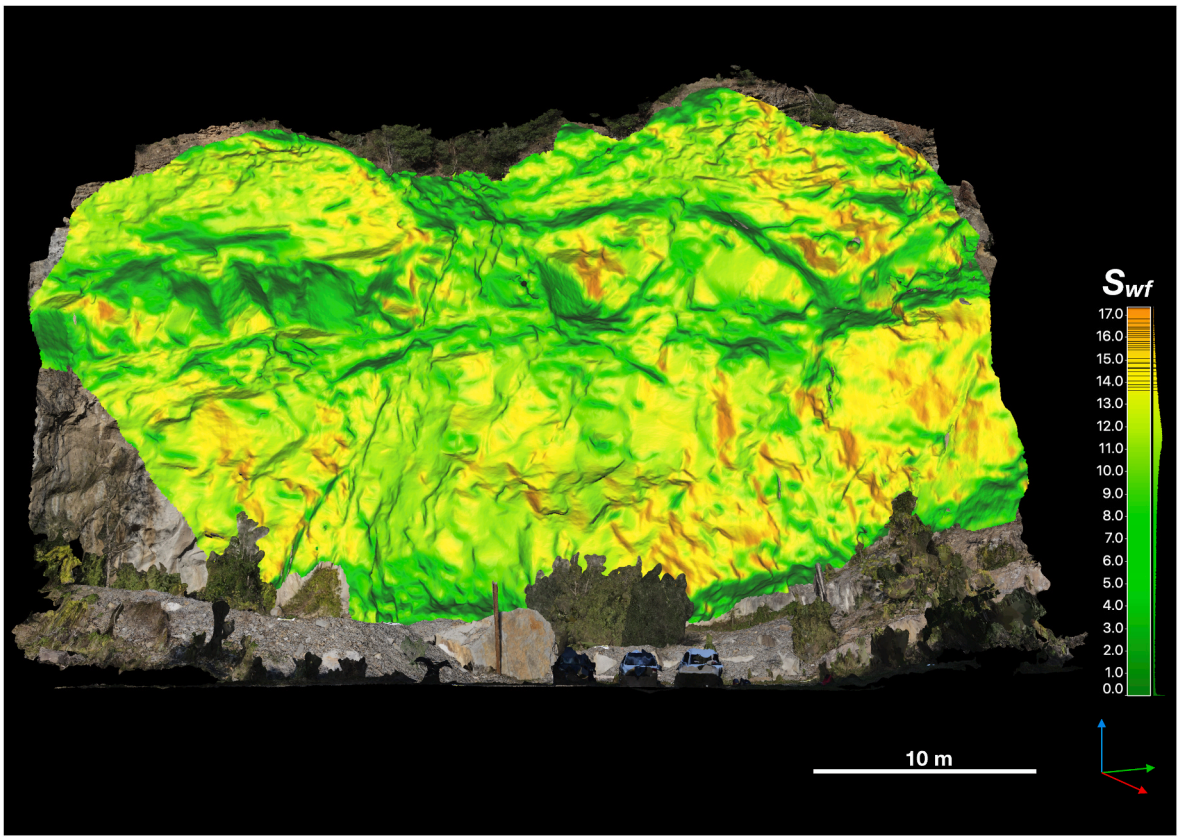

Fig. 9. Calculated susceptibility to rockfalls induced by wedge failure at each element of the polygonal mesh. Results are superimposed on the point cloud of the quarry slope.

depends on the spatial distribution of the computed values as well as the total number of sampled discontinuities and intersections. The procedure is not to be seen as a replacement for field observations and geomechanical analysis of single rock compartments, which are essential for examining the continuity of highly susceptible areas, the presence of weak structures, and the size of potential instabilities. Moreover, the role played by external factors in promoting rockfalls (e.g., rainfall, freeze-thaw, seismic activity, wind-induced leverage by tree roots) is necessarily neglected.

Fig. 7 shows the contour plot of the poles to discontinuities (equal angle, lower hemisphere projection) extracted from application of the DiAna routine at the quarry test site. It should be noted that the classification into discontinuity sets is for illustrative purposes and does not have any influence on Diana-K. The results of the rockfall susceptibility assessment are then shown in Figs. 8–11. A dynamic perspective of the quarry slope, intermittently overlain by the computed maps of susceptibility to the different failure mechanisms, is also provided in Supplementary Videos S1–S4. It is interesting to note that wedge (Fig. 9 and Supplementary Video S2) and flexural toppling failure (Fig. 10 and Supplementary Video S3) appear to be more likely from a spatial perspective, as related indexes of susceptibility (S_{wf} and S_{ftf}) exceed 10% in much of the rock wall area. However, as regards absolute values, indexes of susceptibility exceeding 20% are only produced by the plane (S_{pf}, Fig. 8 and Supplementary Video S1) and free fall mechanisms (S_{fff}, Fig. 11 and Supplementary Video S4). These are concentrated in small and extremely steep areas of the rock wall. Results for block toppling are not depicted because related values of susceptibility (S_{btf}) are always lower than 1%. Fig. 12 indicates how different failure mechanisms may be more likely in different parts of the rock wall: the single mesh elements are in fact colored based on the susceptibility index that locally acquires the greatest value, granted that at least one of them exceeds 1% (i.e., mesh elements are grayed out if no associated index of susceptibility exceeds 1%). This confirms that wedge failure, and secondarily flexural toppling, are statistically prevalent (comparatively higher S_{wf} and S_{ftf}) at most points of the rock face, with the latter often being confined to the lower half of the slope.

Supplementary data related to this article can be found at https://doi.org/10.1016/j.ijrmms.2022.105178.

Validation of a procedure for rockfall susceptibility assessment may be carried out in two ways: by direct observation of several rockfall events and comparison of their source location with the predicted areas of greater hazard; or by visual inspection of the rock wall to confirm whether the predicted structures are actually identifiable at the surface. The first approach may be very time consuming, as many years may need to pass before a sufficient number of detectable rockfalls occur. Since the investigated rock wall is of limited size and easily accessible, ground-truthing was deemed as an efficient mean for results validation. With the exception of the unlikely block toppling mechanism, some illustrative photographs are provided as insets to Fig. 12. These demonstrate that areas of higher computed susceptibility are consistent with the presence of block geometries that are evidently prone to the predicted mode of failure. It is also worth mentioning that high values of susceptibility to free fall and wedge failure are located in proximity of an overhanging area of the rock wall that was affected by a rockfall of approximately 100 m^3 few years prior to the survey (panel '*a*' in Fig. 12).

4. Discussion

Thorough quantification of rockfall hazards is strictly dependent on realistic sampling of discontinuity and rock face orientations. In this sense, the proposed Diana-K approach is founded on the ability of TLS to produce three-dimensional representations of the observed scenario by measuring with millimetric to centimetric accuracy the distance of a regular pattern of millions of points in a polar coordinate system. With

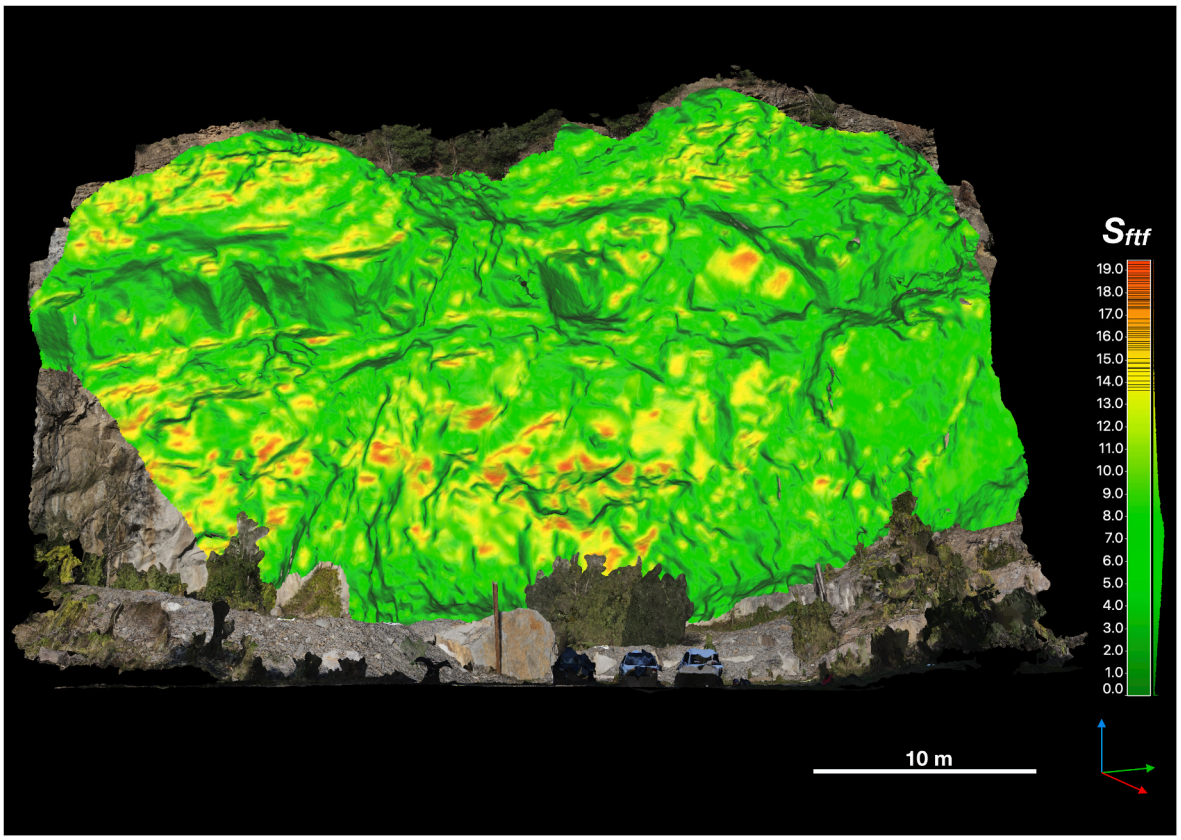

Fig. 10. Calculated susceptibility to rockfalls induced by flexural toppling failure at each element of the polygonal mesh. Results are superimposed on the point cloud of the quarry slope.

the ever increasing availability of computing power, the extraction of discontinuity orientations directly from raw point cloud data (as done in DiAna) is a definite advantage with respect to mesh-based applications, whose quality can be influenced by the distortion of polygonal surfaces in the triangulation process.[24] In Diana-K, rockfall susceptibility is subsequently assessed in similar semi-automatic manner on the basis of stereographic-based kinematic analysis, hence it is treated as a geometric problem solely driven by rock mass structure and rock face orientation. Complex geometries involving multiple basal, rear, and lateral release surfaces are not taken into consideration. The analysis also excludes processes of intact rock fracture and external forces such as water pressures or reinforcement, which can significantly influence stability. Design procedures should entail preliminary kinematic analysis to identify where the conditions for block sliding or rotation are more pronounced, and then focused deterministic/stress-strain analysis to infer local factors of safety.[41]

Predictions of kinematic instability have mostly been carried out in previous studies by combining the orientation of mesh elements (or point cloud data) with the mean orientation of discontinuity sets.[21,46] This is a major simplification with respect to the natural scatter of discontinuity orientations in rock masses. To better deal with the issue, some authors[47,48] proposed to treat discontinuity orientation as a random variable, as for example in a Monte Carlo framework. These works proved that, in rough rock faces with markedly non-uniform orientation, little variations in input structural data may lead to kinematic evaluations significantly biased towards unsafety. Diana-K overcomes the uncertainties inherent to modeling the distribution of discontinuity orientations, since these are comprehensively sampled from TLS data. Probabilistic context is rather provided by coupling iteratively each mesh element with the orientation of each mapped discontinuity/intersection (or possible combination thereof). It is therefore assumed that any mapped discontinuity/intersection may intersect a given point of the rock face. Local susceptibility to a certain mode of failure is consequently expressed by the relative amount of features theoretically able to satisfy the associated kinematic requirements.

The Diana-K routine also allows incorporation of additional spatial arguments by assigning distinct weighting factors (D_w) to the discontinuity planes inputted at each iteration step of kinematic analysis. This is aimed at yielding results that better reflect local rock mass conditions, and is achieved by measuring the distance (D) between the center of gravity of the discontinuity planes and the center of gravity of the mesh element under analysis. On the basis of two user-defined parameters, namely threshold distance (T_d) and maximum weight (M_w), the probabilistic role played by a discontinuity in increasing rockfall susceptibility at a given element of the polygonal mesh is estimated by rounding towards the nearest integer the following equation:

$$D_w = M_w[(T_d - D) / T_d] \tag{39}$$

Eq. (39) indicates that discontinuities located at a distance from the analyzed mesh element greater than T_d are excluded from related calculations of rockfall susceptibility. Conversely, discontinuities located at a distance equal to or shorter than T_d appear in the input sample as many times as the weighting factor D_w. This adjustment is justified especially for large rock walls, where different structural domains may prevail in different sectors of the point cloud. Similarly, instead of exploiting values that are averaged for each discontinuity set (as done in this study), field observations may motivate the assignment of specific friction angles to highly weathered or damaged discontinuities of substantially weaker strength.

Even though the presented quarry test site is characterized by a relatively straightforward jointing pattern, the results highlight the importance of properly addressing the sub-vertical nature of rock walls. While the kinematic feasibility of wedge and flexural toppling failure is

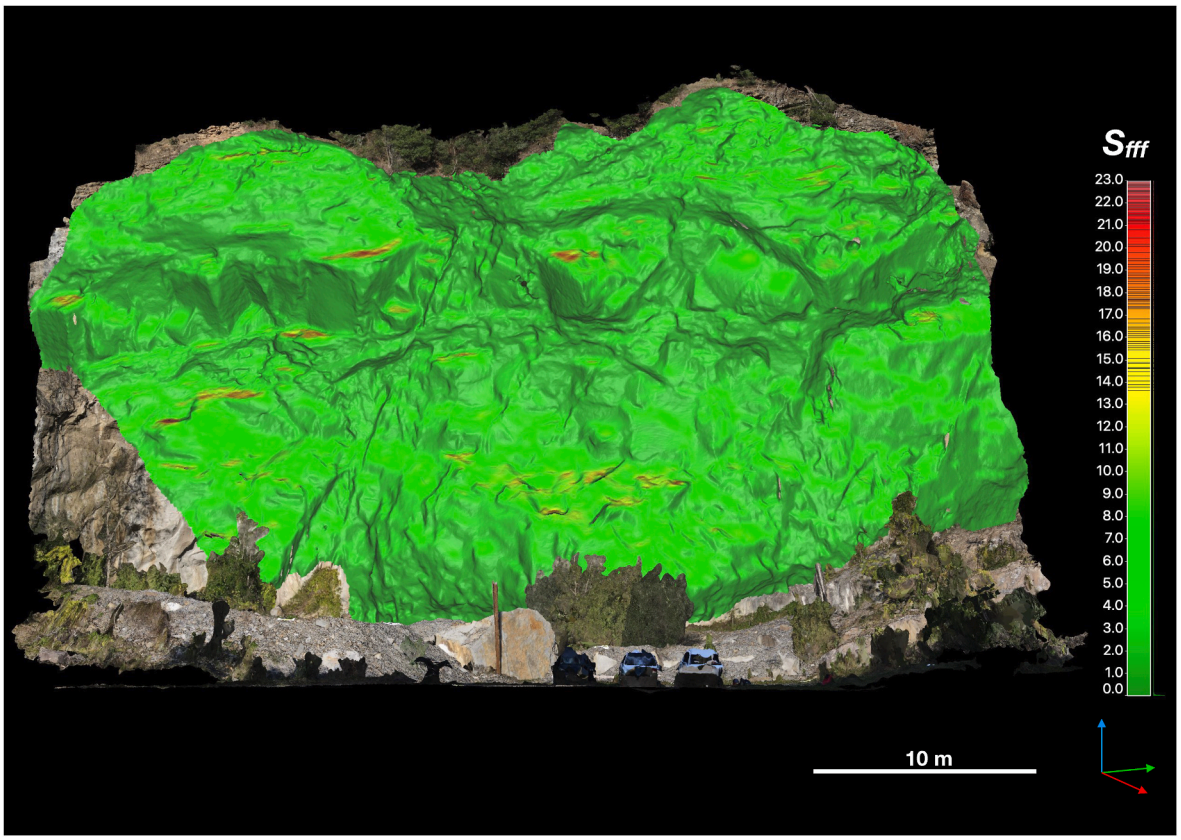

Fig. 11. Calculated susceptibility to rockfalls induced by free fall failure at each element of the polygonal mesh. Results are superimposed on the point cloud of the quarry slope.

comparatively dominant over most portions of the surveyed face, in absolute terms the highest hazard is attributed to plane and free fall mechanisms potentially originating from highly steep areas of limited extent. This kind of distinction, related to the presence of small-scale overhangs, may not be obtained from traditional methods of rockfall hazard assessment that employ airborne-based digital elevation models.[10,20,49,50] On a similar note, Matasci et al.[21] stressed the impact of exfoliation-type discontinuities (i.e., discontinuities that are sub-parallel to the rock face) on rockfall susceptibility in granitic and debuttressed hard rock masses. In cases where the probability of failure related to exfoliation discontinuities is relevant, a module of the Diana-K routine can be switched on to calculate an "*exfoliation susceptibility index*": this serves to count how many discontinuity planes have a dip within a predefined range (e.g., $\pm 10°$) from the dip of a given element of the polygonal mesh.

Another relevant information is the assessment of the overall susceptibility to rockfalls, regardless of mode of failure. It is in fact reasonable to expect that rockfalls will be more frequent in areas where kinematic freedom is achievable through multiple block geometries. Overall rockfall susceptibility can be captured by a Global Kinematic Index (GKI):

$$GKI = 1 - \left(1 - S_{pf} - N_{fff} - S_{ft}\right)\left(1 - S_{wf} - I_{fff}\right)\left(1 - S_{btf}\right) \tag{40}$$

where symbols have already been introduced in previous equations. The first term in parenthesis defines the contribution to rockfall susceptibility from the unfavorable orientation of discontinuity planes, the second term by the unfavorable orientation of lines of intersection, and the third term is solely descriptive of block toppling since this mechanism is simultaneously controlled by both planes and intersections. Results from GKI calculation at the quarry test site imply that, in the most critical area of the rock wall (i.e., the mesh element where GKI is highest), 43% of the inputted structural features are theoretically able to promote at least one mechanism of kinematic instability (Fig. 13 and Supplementary Video S5). Illustrative photos in Fig. 13 highlight that multiple feasible modes of failure, conspicuous rock mass damage, and freshly exposed rockfall scars can be discerned in areas of high GKI.

With reference to active surface mining operations and artificial slopes in general, another implication of the proposed procedure is that it offers a framework to search for the geometric configuration of the excavation that best minimizes rockfall hazards. A sensitivity analysis can be performed to understand how indexes of rockfall susceptibility are influenced by the dip and dip direction of the cut face. For example, variations of GKI may be examined by hypothesizing different dip increments for a fixed dip direction of the cut face; or alternatively, by hypothesizing different dip direction increments for a fixed dip of the cut face.[28] This is particularly relevant in open-pit mines: as cut faces take the full range of possible dip directions, their dip may be adjusted from one pit sector to the other in order to meet a targeted level of safety. Knowledge of feasible instability mechanisms is also informative for interpreting the geometry of slope movement vectors, which in turn can significantly affect the measurement accuracy of line-of-sight slope monitoring techniques such as ground-based interferometric radar.[51] Displacement/velocity data may be corrected by estimating the sensitivity of the sensor against the estimated direction of slope movement, thus providing valuable context for the appropriate assessment of ongoing instabilities and the calibration of related alarms.

5. Conclusions

The presented analysis workflow is concerned with the thorough quantification of rockfall hazards from remotely sensed surface data. It exploits semi-automatic routines for the extraction of discontinuity planes (DiAna) as well as the assessment of structurally controlled

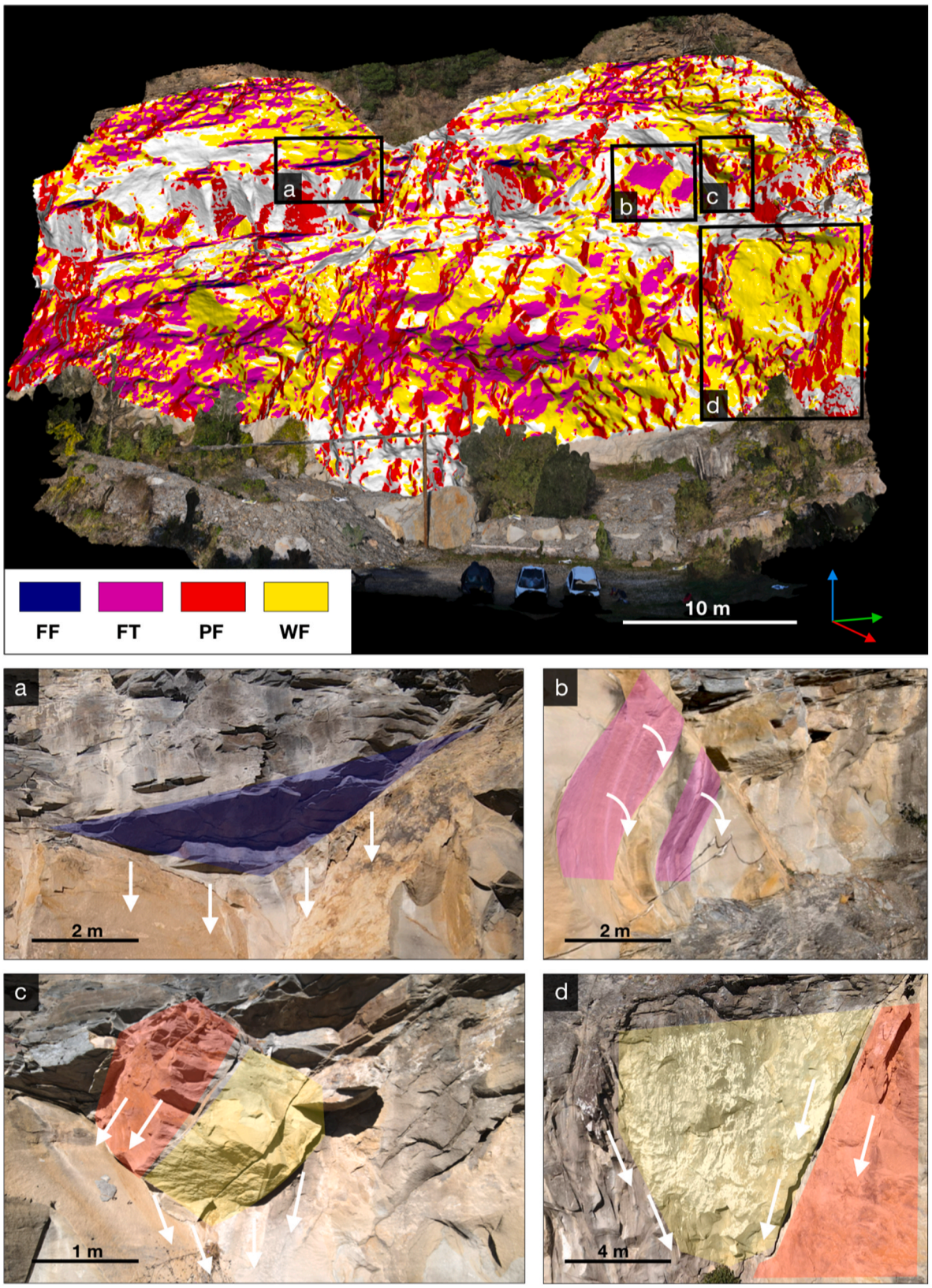

Fig. 12. Estimation of the most likely mode of failure at each element of the polygonal mesh. Results are superimposed on the point cloud of the quarry slope. FF = free fall; FT = flexural toppling; WF = wedge failure; PF = plane failure.

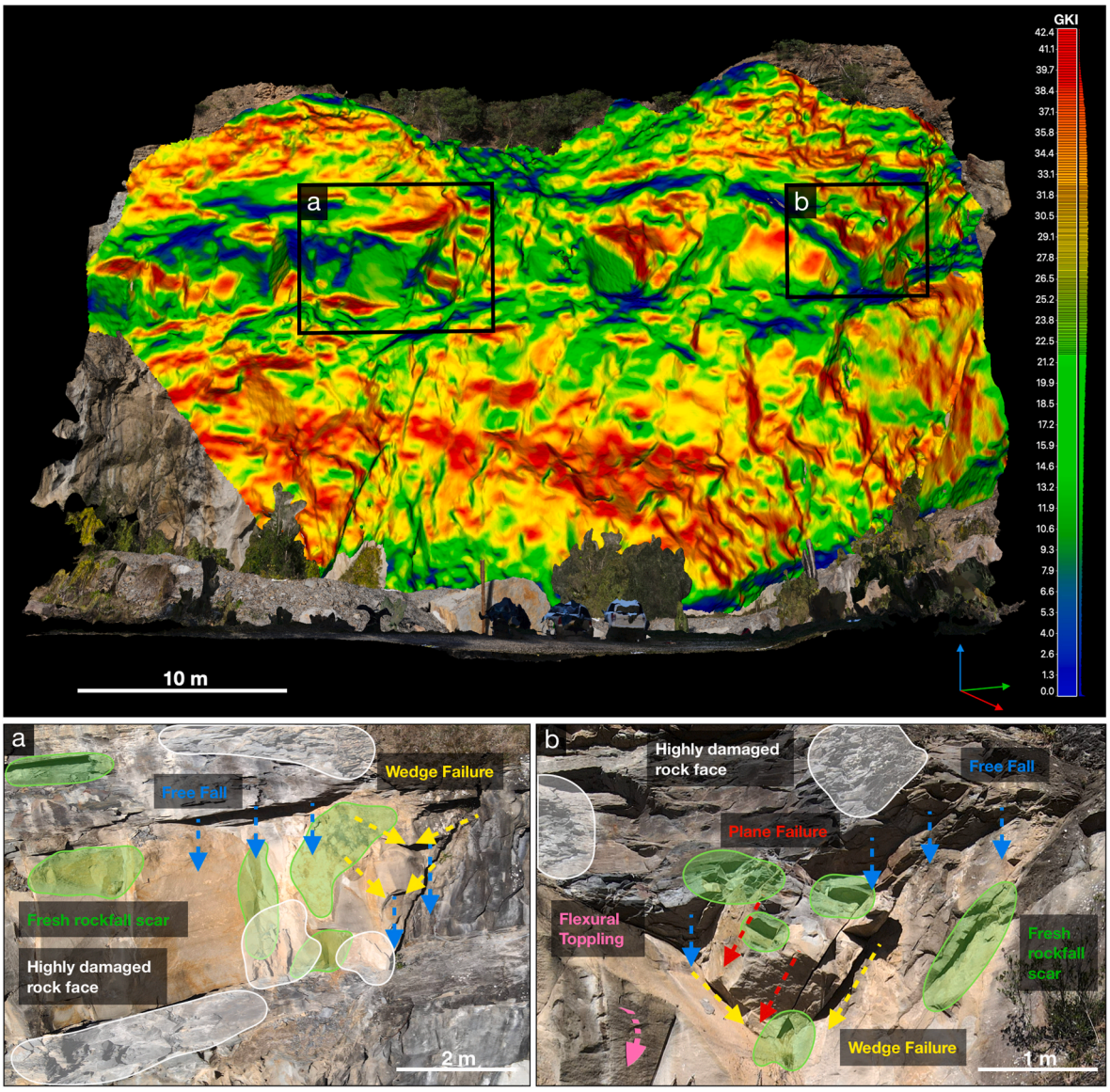

Fig. 13. Calculated global susceptibility to rockfalls at each element of the polygonal mesh, regardless of mode of failure (GKI index). Results are superimposed on the point cloud of the quarry slope. Panels a) and b): zoomed in photos of areas within the respective black boxes in the main figure, exemplifying that multiple feasible mechanisms of block detachment, rock mass damage, and recent rockfall scars are apparent in areas of higher GKI.

rockfall susceptibility scenarios (DiAna-K). The procedure is not to be viewed as a univocal replacement for traditional geomechanical surveying, but rather as an approach that becomes an inevitable necessity to practitioners who must collect data in vast, dangerous, or otherwise inaccessible environments. Potential modes of failure identified at the quarry test site agree well with evidences gathered in the field, with the added benefit given by the ability to rapidly investigate areas of large extent and marked steepness—including truly overhanging rock faces. Further steps, among which the possibility to assign spatial weighting and distinct friction angles, can be taken to better incorporate the characteristics of single discontinuities/intersections into the analysis of complex scenarios. Further verification of the method could be conducted by integrating the kinematic analysis outputs with spatially continuous slope deformation data or detailed rockfall inventories at sites of frequent rockfall occurrence, with the goal of deriving explicit correlations between statistically likely (i.e., predicted) and actually ongoing instabilities. The code implemented into the Diana and Diana-K routines may be promptly run on a MATLAB environment even by users who do not possess advanced programming skills.

Declaration of competing interest

The authors declare that they have no known competing financial interests or personal relationships that could have appeared to influence the work reported in this paper.

Appendix A. Supplementary data

Supplementary data to this article can be found online at https://doi.org/10.1016/j.ijrmms.2022.105178.

References

1 Hungr O, Leroueil S, Picarelli L. The Varnes classification of landslide types, an update. *Landslides*. 2014;11:167–194. https://doi.org/10.1007/s10346-013-0436-y.
2 Evans SG, Hungr O. The assessment of rockfall hazard at the base of talus slopes. *Can Geotech J*. 1993;30:620–636. https://doi.org/10.1139/t98-106.
3 Luckman BH. Processes, transport, deposition, and landforms: rockfall. In: Shroder JF, ed. *Treatise on Geomorphology*. San Diego, CA: Elsevier; 2013:174–182.

4 Corominas J, Mavrouli O, Ruiz-Carulla R. Magnitude and frequency relations: are there geological constraints to the rockfall size? *Landslides*. 2018;15:829–845. https://doi.org/10.1007/s10346-017-0910-z.

5 Abellán A, Calvet J, Vilaplana JM, Blanchard J. Detection and spatial prediction of rockfalls by means of terrestrial laser scanner monitoring. *Geomorphology*. 2010;119:162–171. https://doi.org/10.1016/j.geomorph.2010.03.016.

6 Mazzanti P, Bozzano F, Cipriani I, Prestininzi A. New insights into the temporal prediction of landslides by a terrestrial SAR interferometry monitoring case study. *Landslides*. 2015;12:55–68. https://doi.org/10.1007/s10346-014-0469-x.

7 Carlà T, Nolesini T, Solari L, Rivolta C, Dei Cas L, Casagli N. Rockfall forecasting and risk management along a major transportation corridor in the Alps through ground-based radar interferometry. *Landslides*. 2019;16:1425–1435. https://doi.org/10.1007/s10346-019-01190-y.

8 Duarte RM, Marquínez J. The influence of environmental and lithologic factors on rockfall at a regional scale: an evaluation using GIS. *Geomorphology*. 2002;43(1–2):117–136. https://doi.org/10.1016/S0169-555X(01)00126-X.

9 Frattini P, Crosta G, Carrara A, Agliardi F. Assessment of rockfall susceptibility by integrating statistical and physically-based approaches. *Geomorphology*. 2008;94(3–4):419–437. https://doi.org/10.1016/j.geomorph.2006.10.037.

10 Loye A, Jaboyedoff M, Pedrazzini A. Identification of potential rockfall source areas at a regional scale using a DEM-based geomorphometric analysis. *Nat Hazards Earth Syst Sci*. 2009;9:1643–1653. https://doi.org/10.5194/nhess-9-1643-2009.

11 Michoud C, Derron M-H, , et alQueyrel A. Rockfall hazard and risk assessments along roads at a regional scale: example in Swiss Alps. *Nat Hazards Earth Syst Sci*. 2012;12:615–629. https://doi.org/10.5194/nhess-12-615-2012.

12 Dunham L, Wartman J, Olsen MJ, O'Banion M, Cunningham K. Rockfall Activity Index (RAI): a lidar-derived, morphology-based method for hazard assessment. *Eng Geol*. 2017;221:184–192. https://doi.org/10.1016/j.enggeo.2017.03.009.

13 Hungr O, Evans SG, Hazzard J. Magnitude and frequency of rock falls and rock slides along the main transportation corridors of southwestern British Columbia. *Can Geotech J*. 1999;36:224–238. https://doi.org/10.1139/t98-106.

14 Dussauge C, Grasso J-R, Helmstetter A. Statistical analysis of rockfall volume distributions: implications for rockfall dynamics. *J Geophys Res Solid Earth*. 2003;108(B6):2286. https://doi.org/10.1029/2001JB000650.

15 Macciotta R, Hendry M, Cruden DM, Blais-Stevens A, Edwards T. Quantifying rock fall probabilities and their temporal distribution associated with weather seasonality. *Landslides*. 2017;14:2025–2039. https://doi.org/10.1007/s10346-017-0834-7.

16 Pratt C, Macciotta R, Hendry H. Quantitative relationship between weather seasonality and rock fall occurrences north of Hope, BC, Canada. *Bull Eng Geol Environ*. 2019;78:3239–3251. https://doi.org/10.1007/s10064-018-1358-7.

17 Melzner S, Rossi M, Guzzetti F. Impact of mapping strategies on rockfall frequency-size distributions. *Eng Geol*. 2020;272, 105639. https://doi.org/10.1016/j.enggeo.2020.105639.

18 Jaboyedoff M, Baillifard F, Philippossian F, Rouiller JD. Assessing fracture occurrence using weighted fracture density: a step towards estimating rock instability. *Nat Hazards Earth Syst Sci*. 2004;4:83–93. https://doi.org/10.5194/nhess-4-83-2004.

19 Brideau M-A, Pedrazzini A, Stead D, Froese C, Jaboyedoff M, van Zeyl D. Three-dimensional slope stability analysis of south peak, crowsnest pass, alberta, Canada. *Landslides*. 2011;8:139–158. https://doi.org/10.1007/s10346-010-0242-8.

20 Guenther A, Wienhöfer J, Konietzky H. Automated mapping of rock slope geometry, kinematics and stability with RSS-GIS. *Nat Hazards*. 2012;61:29–49. https://doi.org/10.1007/s11069-011-9771-2.

21 Matasci B, Stock GM, Jab, , et alRavanel L. Assessing rockfall susceptibility in steep and overhanging slopes using three-dimensional analysis of failure mechanisms. *Landslides*. 2018;15:859–878. https://doi.org/10.1007/s10346-017-0911-y.

22 Abellán A, Oppikofer T, Jaboyedoff M, Rosser NJ, Lim M, Lato MJ. Terrestrial laser scanning of rock slope instabilities. *Earth Surf Process Landforms*. 2014;39:80–97. https://doi.org/10.1002/esp.3493.

23 Stead D, Donati D, Wolter A, Sturzenegger M. Application of remote sensing to the investigation of rock slopes: experience gained and lessons learned. *Int J Geo-Inf*. 2019;8:296. https://doi.org/10.3390/ijgi8070296.

24 Battulwar R, Zare-Naghadehi M, Emami E, Sattarvand J. A state-of-the-art review of automated extraction of rock mass discontinuity characteristics using three-dimensional surface models. *J Rock Mech Geotech Eng*. 2021;13(4):920–936. https://doi.org/10.1016/j.jrmge.2021.01.008.

25 Sturzenegger M, Stead D. Close-range terrestrial digital photogrammetry and terrestrial laser scanning for discontinuity characterization on rock cuts. *Eng Geol*. 2009;106:163–182. https://doi.org/10.1016/j.enggeo.2009.03.004.

26 Vöge M, Lato MJ, Diederichs MS. Automated rockmass discontinuity mapping from 3-dimensional surface data. *Eng Geol*. 2013;164:155–162. https://doi.org/10.1016/j.enggeo.2013.07.008.

27 Riquelme AJ, Abellán A, Tomás R, Jaboyedoff M. A new approach for semi-automatic rock mass joints recognition from 3D point clouds. *Comput Geosci*. 2014;68:38–52. https://doi.org/10.1016/j.cageo.2014.03.014.

28 Casagli N, Pini G. Analisi cinematica della stabilità di versanti naturali e di fronti di scavo in roccia (in Italian). *Geol Appl Idrogeol*. 1993;28:223–232.

29 Gigli G, Casagli N. Semi-automatic extraction of rock mass structural data from high resolution LIDAR point clouds. *Int J Rock Mech Min Sci*. 2011;48:187–198.

30 Fanti R, Gigli G, Lombardi L, Tapete D, Canuti P. Terrestrial laser scanning for rockfall stability analysis in the cultural heritage site of Pitigliano (Italy). *Landslides*. 2013;10:409–420. https://doi.org/10.1007/s10346-012-0329-5.

31 Gigli G, Frodella W, , et alombardi L. Instability mechanisms affecting cultural heritage sites in the Maltese Archipelago. *Nat Hazards Earth Syst Sci*. 2012;12:1883–1903. https://doi.org/10.5194/nhess-12-1883-2012.

32 Gigli G, Morelli S, Fornera S, Casagli N. Terrestrial laser scanner and geomechanical surveys for the rapid evaluation of rock fall susceptibility scenarios. *Landslides*. 2014;11:1–14. https://doi.org/10.1007/s10346-012-0374-0.

33 Gigli G, Frodella W, Gar, , et alCasagli N. 3-D geomechanical rock mass characterization for the evaluation of rockslide susceptibility scenarios. *Landslides*. 2014;11:131–140. https://doi.org/10.1007/s10346-013-0424-2.

34 Frodella W, Ciampalini A, , et alCasagli N. Synergic use of satellite and ground based remote sensing methods for monitoring the San Leo rock cliff (Northern Italy). *Geomorphology*. 2016;264:80–94. https://doi.org/10.1016/j.geomorph.2016.04.008.

35 Frodella W, Elashvili M, Spiz, , et alCasagli N. Applying close range non-destructive techniques for the detection of conservation problems in rock-carved cultural heritage sites. *Rem Sens*. 2021;13(5):1040. https://doi.org/10.3390/rs13051040.

36 Goodman RE. *Methods of Geological Engineering in Discontinuous Rocks*. West Publishing Company; 1976.

37 Hoek E, Bray JW. *Rock Slope Engineering*. 3ed ed. London, UK: Institution of Mining and Metallurgy; 1981.

38 Matheson GD. *Rock Stability Assessment in Preliminary Site Investigation — Graphical Methods*. Wokingham, UK: Transport and Road Research Laboratory; 1983.

39 Matheson GD. The collection and use of field discontinuity data in rock slope design. *Q J Eng Geol*. 1989;22:19–30. https://doi.org/10.1144/GSL.QJEG.1989.022.01.02.

40 Hudson JA, Harrison JP. *Engineering Rock Mechanics: An Introduction to the Principles*. second ed. Oxford, UK: Elsevier; 2000.

41 Wyllie DC, Mah CW. *Rock Slope Engineering*. fourth ed. New York, NY: Spon Press; 2004.

42 ISRM (International Society for Rock Mechanics). Suggested methods for the quantitative description of discontinuities in rock masses. *Int J Rock Mech Min Sci Geomech Abstr*. 1978;15:319–368.

43 Maksimović M. The shear strength components of a rough rock joint. *Int J Rock Mech Min Sci Geomech Abstr*. 1996;33(8):769–783.

44 Barton N, Choubey V. The shear strength of rock joints in theory and practice. *Rock Mech*. 1977;10:1–54.

45 Cruden DM. Limits to common toppling. *Can Geotech J*. 1989;26:737–742. https://doi.org/10.1139/t89-085.

46 Robiati C, Eyre M, Vanneschi C, Francioni M, Venn A, Coggan J. Application of remote sensing data for evaluation of rockfall potential within a quarry slope. *Int J Geo-Inf*. 2019;8:367. https://doi.org/10.3390/ijgi8090367.

47 Park H-J, Lee J-H, Kim K-M, Um J-G. Assessment of rock slope stability using GIS-based probabilistic kinematic analysis. *Eng Geol*. 2016;203:56–69.

48 Zheng J, Kulatilake PHSW. Improved probabilistic kinematic analysis procedure based on finite size discontinuities and its application to a rock slope at open pit mine in U.S. *Int J GeoMech*. 2017;17(2), 04016052.

49 Lan H, Martin CD, Zhou C, Lim CH. Rockfall hazard analysis using LiDAR and spatial modeling. *Geomorphology*. 2010;118:213–223. https://doi.org/10.1016/j.geomorph.2010.01.002.

50 Messenzehl K, Meyer H, Otto J-C, Hoffmann T, Dikau R. Regional-scale controls on the spatial activity of rockfalls (Turtmann Valley, Swiss Alps) — a multivariate modeling approach. *Geomorphology*. 2017;287:29–45. https://doi.org/10.1016/j.geomorph.2016.01.008.

51 Farina P, Bardi F, Lombardi L, Gigli G. Combining structural data with monitoring data in open pit mines to interpret the failure mechanism and calibrate radar alarms. In: Dight PM, ed. *Proceedings of the 2020 International Symposium on Slope Stability in Open Pit Mining and Civil Engineering*. Perth, WA: Australian Centre for Geomechanics; 2020:523–534. https://doi.org/10.36487/ACG_repo/2025_31.